14th International Symposium on Turbulence and Shear Flow Phenomena (TSFP14)
Heidelberg, Germany, July 28–31, 2026

MITIGATING FLASHBACK RISK WITH AUTOMATIC BOUNDARY CONDITION AND MESH-DEFORMING SHAPE OPTIMIZATION

Kai Hildebrandt
Flow Instabilities and Dynamics
Technische Universität Berlin
k.hildebrandt@tu-berlin.de

Alexander Jaeschke
Chair of Fluid Dynamics
Technische Universität Berlin

Olivier Marquet
Department of Aerodynamics, Aeroelasticity and Acoustics (DAAA)
ONERA – The French Aerospace Lab
Institut Polytechnique de Paris

Kilian Oberleithner
Flow Instabilities and Dynamics
Technische Universität Berlin

ABSTRACT

This study investigates the optimization of cold flow in a hydrogen jet burner to mitigate the risk of flashback. The objective of the optimization was to increase the wall-normal velocity gradient in the mixing tube while decreasing the centerline velocity. Two optimization parameters were considered: first, the injection of secondary flow through boundary-condition optimization and second shape optimization. The descent directions were computed from gradient information obtained with incompressible Reynolds-averaged Navier-Stokes simulations, closed by a k-ε turbulence model. The central tool is the newly developed unified framework FlexiRANS, which solves the forward problem and symbolically derives adjoint-based sensitivities of integral quantities in an automatic manner. For shape optimization, mesh quality was preserved by computing mesh deformations based on an analogy to linear elasticity. Differentiable Dirichlet boundary conditions were imposed using Nitsche's method. The paper concludes with preliminary experimental investigations of the shape-optimized mixing tube, which indicate a flashback shift of more than 11% in equivalence ratio relative to the straight baseline tube and thus demonstrate the potential of the proposed approach.

INTRODUCTION

The increasing demand for carbon-free electricity generation and stability of the electrical grid has intensified interest in hydrogen as an energy carrier for gas-turbine applications. However, compared with conventional hydrocarbon fuels, hydrogen exhibits substantially higher reactivity. As a result, hydrogen flames are prone to propagate upstream from the combustion chamber into the premixing section when conventional swirl-stabilized burners are employed. This phenomenon represents a major obstacle to the safe operation of premixed hydrogen combustors.

To reduce the propensity for flashback (FB), hydrogen combustors often rely on jet flames with high axial velocity rather than swirl-stabilized flames. Nevertheless, a critical region remains near the combustor wall, where the local flow velocity is reduced and can fall below the burning velocity. In this case, the flame can propagate upstream within the boundary layer, leading to boundary layer FB. Proposed mitigation strategies include cooling the wall and leaning the mixture in the boundary layer. Another strategy increases the wall-normal gradient of the axial velocity, a key parameter in FB onset (Kalantari & McDonell, 2017).

In this study, this gradient was increased by thinning the boundary layer and altering the flow profile such that it more closely resembles a flow profile with high velocities near the boundary. For this, two classes of control parameters were considered. First, a continuous suction/injection distribution on the wall of the mixing tube was computed that injects momentum into the boundary layer, increasing the local velocities. Second, shape modifications were computed, forming a nozzle shape that increases flow rates near the wall. A preliminary experimental investigation of the shape-optimized mixing tube is presented last.

MEAN FLOW COMPUTATION

Both optimizations were performed for the same baseline configuration, namely a cold jet flow at Re = 7,840, based on nozzle diameter $D = 0.02\,\mathrm{m}$, kinematic viscosity of air $\mu = 1.5\times10^{-5}\,\mathrm{m^2/s}$ and bulk velocity $u_{\mathrm{bulk}} = 5.88\,\mathrm{m/s}$. The computational domain Ω and its boundaries Γ are shown in Fig. 1. They represent a simplified model of the experimental burner used in this study; details of the experimental setup are provided in Jaeschke *et al.* (2026). The forward problem consisted of the incompressible Reynolds-averaged Navier-Stokes (RANS) equations governing the mean flow velocity $\boldsymbol{u}$ and pressure p (Pope, 2015):

$$\rho\boldsymbol{u}\cdot\nabla\boldsymbol{u} = \nabla\cdot\boldsymbol{\sigma}\ , \quad (1)$$

$$\nabla\cdot\boldsymbol{u} = 0\ . \quad (2)$$

The stress tensor

$$\boldsymbol{\sigma}(\boldsymbol{u},p) = -p\mathbf{I} + 2(\mu+\mu_T)\mathrm{sym}(\nabla\boldsymbol{u}) \quad (3)$$

and $\mathrm{sym}(\nabla\boldsymbol{u}) = \frac{1}{2}(\nabla\boldsymbol{u}+\nabla\boldsymbol{u}^{\mathrm{T}})$ is the symmetric part of a second-order tensor.

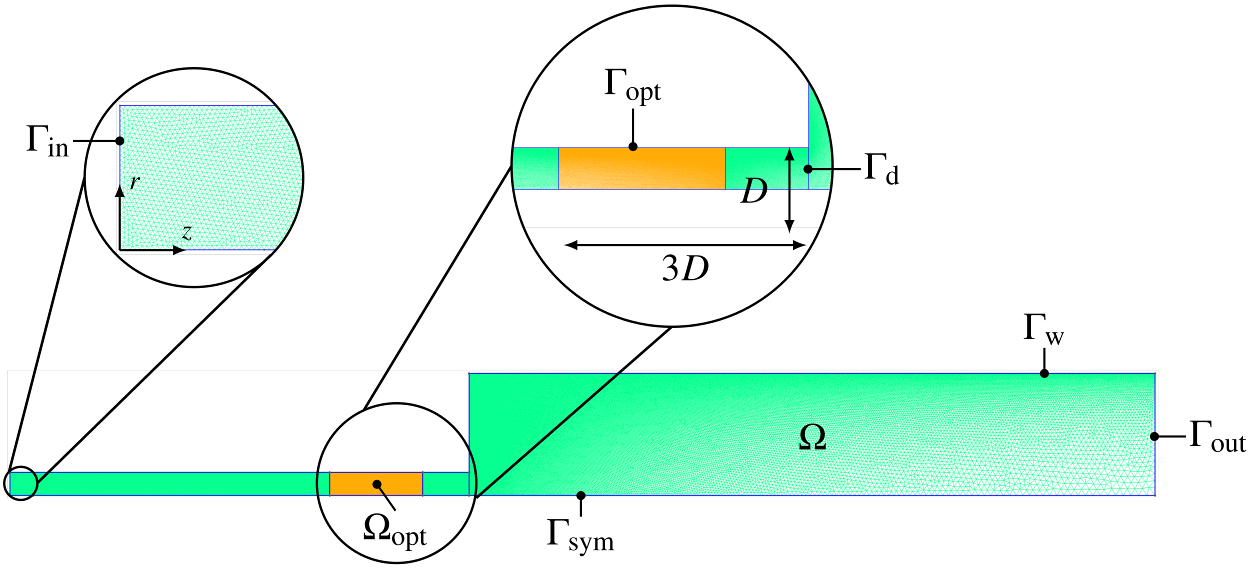

Figure 1: Illustration of the rotationally symmetric computational domain. The close-up on the left-hand side shows the inlet Γ_{in}, the streamwise coordinate z and the radial coordinate r. The close-up on the right-hand side shows the optimized domain Ω_{opt}, optimized boundary Γ_{opt} and distances to the dump plane Γ_{d}. In the experiments, the flame anchors right after Γ_{d} in the combustion chamber.

The RANS equations were closed with the standard k–ε turbulence model (Jones & Launder, 1972), where k is the turbulent kinetic energy, ε the dissipation rate and the turbulent eddy viscosity

$$\mu_T = \rho C_\mu \frac{k^2}{\varepsilon} \,. \tag{4}$$

k and ε are modeled by two advection-diffusion-reaction equations:

$$\rho \boldsymbol{u} \cdot \nabla k - \nabla \cdot \left(\left(\mu + \frac{\mu_T}{\sigma_k} \right) \nabla k \right) = P_k - \rho \varepsilon, \tag{5}$$

$$\rho \boldsymbol{u} \cdot \nabla \varepsilon - \nabla \cdot \left(\left(\mu + \frac{\mu_T}{\sigma_\varepsilon} \right) \nabla \varepsilon \right) = \frac{\varepsilon}{k} \left(C_1 P_k - \rho C_2 \varepsilon \right) , \tag{6}$$

where the production of turbulent kinetic energy

$$P_k = \frac{\mu_T}{2} \left| \nabla \boldsymbol{u} + \nabla \boldsymbol{u}^{\mathrm{T}} \right|^2 . \tag{7}$$

Table 1 lists the constants of the $k - \varepsilon$ model.

Table 1: Default empirical constants of the k–ε model.

C_μ	C_1	C_2	σ_k	σ_ε
0.09	1.44	1.92	1.0	1.3

The flow governing equations are supplemented with boundary conditions (BCs). These were at the walls Γ_{w} and with the outward-facing normal vector $\boldsymbol{n}$

$$\boldsymbol{u} = \boldsymbol{0}, \qquad k = 0, \qquad \frac{\partial \varepsilon}{\partial \boldsymbol{n}} = 0 \qquad \text{on } \Gamma_{\text{w}} \,. \tag{8}$$

At the inlet of the mixing tube Γ_{in} , a quadratic velocity profile was prescribed by $u_z = 4(D/2 - r)^2 / D u_{\text{bulk}}$. Initial conditions for the turbulent variables were selected following the recommendations in the Ansys Fluent User's Guide for fully developed pipe flow (ans, 2009). Near the wall, k decreased quadratically to zero over a distance of $0.01D$ to satisfy the wall condition. With a turbulence intensity $\mathrm{TI} = 0.16 \mathrm{Re}^{-1/8}$ and the size of the largest eddies in the mixing tube $l = 0.07D$, the inlet conditions read:

$$\boldsymbol{u} = \boldsymbol{u}_{\text{in}}, \quad k = \frac{3}{2} \left(u_{\text{bulk}} \mathrm{TI} \right)^2 , \quad \varepsilon = C_\mu^{3/4} \frac{k^{3/2}}{l} \quad \text{on } \Gamma_{\text{in}} \,. \tag{9}$$

At the outlet

$$\nabla \boldsymbol{u} \cdot \boldsymbol{n} = \boldsymbol{0}, \quad p = 0, \quad \frac{\partial k}{\partial \boldsymbol{n}} = 0, \quad \frac{\partial \varepsilon}{\partial \boldsymbol{n}} = 0 \quad \text{on } \Gamma_{\text{out}} \,. \tag{10}$$

A homogeneous Dirichlet BC for u_r and homogeneous Neumann BCs for u_z, p, k and ε were applied at the boundary Γ_{sym} on the axis of symmetry.

Ω was discretized with 170,000 triangular elements for the BC optimization and 250,000 elements for the shape optimization (SO). All variational problems were solved with the finite element software FEniCSx (Baratta *et al.*, 2023). For implementation simplicity, the RANS and closure equations were solved with a monolithic underrelaxed Newton method. Since this approach may yield negative μ_T values and cause solver instabilities (Kuzmin *et al.*, 2007), the optimization was initialized with a solution computed in OpenFOAM (ope, 2024). $\boldsymbol{u}$ was approximated with piecewise quadratic Lagrange elements, while p, k and ε were discretized with linear elements. Linear systems were solved by direct LU factorization through PETSc in parallel. The incompressibility constraint was stabilized with a Grad-Div method.

Once the mean flow field has been computed, the gradient of the cost functional is evaluated as the basis for the optimization.

GRADIENT COMPUTATION

The optimization aimed to modify the velocity profile in the mixing tube near the dump plane Γ_d such that the near-wall velocity increases. This increases the wall-normal gradient of u_z and thins the boundary layer. Defining the desired profile as $\boldsymbol{u}_\mathrm{g}$, a cost functional $J(\boldsymbol{u})$ was introduced to measure the mismatch between $\boldsymbol{u}$ and $\boldsymbol{u}_\mathrm{g}$. This results in a tracking-type optimization problem constrained by the nonlinear forward system Eqs. (1), (2), (5) and (6), written compactly as $\boldsymbol{N}(\boldsymbol{q}) = \boldsymbol{0}$:

$$\min_{\boldsymbol{a}\in\mathcal{A}} J(\boldsymbol{u}) = \int_{\Gamma_\mathrm{d}} |\boldsymbol{u}_\mathrm{g} - \boldsymbol{u}|^2 \mathrm{d}s \quad \text{s.t.} \quad \boldsymbol{N}(\boldsymbol{q}) = \boldsymbol{0} \,. \tag{11}$$

Here $\boldsymbol{a}$ are the parameters inside an admissible set $\mathcal{A}$. The goal profile stems from an analytic relation for turbulent pipe flow at Re = 100,000, i.e., about ten times the operational Re of the burner (Salama, 2021). This optimization problem was solved with two types of parameters:

- A suction/injection distribution of fluid on the walls of the mixing tube, i.e., here $\boldsymbol{a} = \boldsymbol{u}_\mathrm{BC}$, a Dirichlet BC on Γ_opt.
- Shape modifications of the mixing tube, i.e., here $\boldsymbol{a} = \boldsymbol{X}$, the mesh nodes in Ω_opt and on Γ_opt.

The question is now how to change $\boldsymbol{a}$ to decrease J. For this, the gradient (or sensitivity) $\frac{dJ}{d\boldsymbol{a}}$ was followed iteratively as it yields a guaranteed direction of descent for small enough changes in the parameters. In general, $J = J(\boldsymbol{a}, \boldsymbol{q}(\boldsymbol{a}))$, e.g., since in shape optimization a perturbation of Ω may change both the state $\boldsymbol{q}$ and the domain of integration of J. Then

$$\frac{dJ}{d\boldsymbol{a}} = \frac{\partial J}{\partial \boldsymbol{a}} + \frac{\partial J}{\partial \boldsymbol{q}}\frac{\partial \boldsymbol{q}}{\partial \boldsymbol{a}} \,. \tag{12}$$

Computing $\frac{\partial \boldsymbol{q}}{\partial \boldsymbol{a}}$ by finite differences is prohibitively expensive because it requires one forward solve for each parameter. This cost can be avoided by introducing the adjoint variables $\boldsymbol{\lambda}$ (Cossu, 2014), which satisfy a linear PDE

$$\left(\frac{\partial \boldsymbol{N}}{\partial \boldsymbol{q}}\right)^\mathrm{T} \boldsymbol{\lambda} = \frac{\partial J}{\partial \boldsymbol{q}} \,. \tag{13}$$

This allows to compute the gradient at roughly the cost of solving the linearized forward system

$$\frac{dJ}{d\boldsymbol{a}} = \frac{\partial J}{\partial \boldsymbol{a}} - \boldsymbol{\lambda}^\mathrm{T}\frac{\partial \boldsymbol{N}}{\partial \boldsymbol{q}} \,. \tag{14}$$

A major difficulty in gradient-based optimization is the derivation of the derivatives appearing in Eqs. (13) and (14). The error-prone manual derivation can be avoided by using automatic tools, of which we chose a symbolic derivation that relies on the Unified Form Language (UFL) (Alnæs *et al.*, 2014), a sub-package of FEniCSx. The resulting continuous adjoint equations were discretized using the same function spaces as the forward system.

With this at hand, the optimization can be summarized as shown in Alg. 1 using a steepest descent method with a fixed step size η. An additional projection of the gradient was computed. Regarding the BC optimization, this was a H^1 projection to ensure smoothness. For the SO, special metrics have to be employed that will be discussed later.

Algorithm 1 Optimization loop

1: **Input:** Ω, $\boldsymbol{N}(\boldsymbol{a},\boldsymbol{q})$, $J(\boldsymbol{a},\boldsymbol{q})$, $\boldsymbol{a}$, step size η
2: **while** not converged **do**
3: Solve forward: $\boldsymbol{q} \leftarrow \boldsymbol{N}(\boldsymbol{q}) = \boldsymbol{0}$
4: Solve adjoint: $\boldsymbol{\lambda} \leftarrow \frac{\partial \boldsymbol{N}}{\partial \boldsymbol{q}}^\mathrm{T} \boldsymbol{\lambda} = \frac{\partial J}{\partial \boldsymbol{q}}$
5: Project gradient: $a_\Omega(\boldsymbol{g}, \boldsymbol{v}) = \frac{dJ}{d\boldsymbol{a}} \cdot \boldsymbol{v}$
6: Update parameters: $\boldsymbol{a} \leftarrow \boldsymbol{a} - \eta \boldsymbol{g}$
7: **end while**

BOUNDARY CONDITION OPTIMIZATION

Methods

The general adjoint-based optimization framework was first applied to boundary condition optimization. Here, the suction/injection profile $\boldsymbol{u} = \boldsymbol{u}_\mathrm{BC}$ on Γ_opt was optimized to reduce J. To enable automatic symbolic differentiation in UFL, the optimization parameter must appear explicitly in the weak form of the governing equations. This is not the case for strongly imposed Dirichlet BCs. Therefore, the BC was enforced weakly using a symmetric Nitsche method (see, e.g., Kontogiannis *et al.*, 2025). This method adds to the naturally arising boundary part (Eq. (15)) a symmetrizing term (Eq. (16)) and a penalty term (Eq. (17)) weighted with $\gamma_\mathrm{N} = 20$. With this, the boundary integrals of the weak form of the RANS equations read:

$$-\int_{\Gamma_\mathrm{opt}} \boldsymbol{n} \cdot \boldsymbol{\sigma}(\boldsymbol{u}, p) \cdot \boldsymbol{v} \mathrm{d}s \tag{15}$$

$$-\int_{\Gamma_\mathrm{opt}} \boldsymbol{n} \cdot \boldsymbol{\sigma}(\boldsymbol{v}, q) \cdot (\boldsymbol{u} - \boldsymbol{u}_\mathrm{BC}) \mathrm{d}s \tag{16}$$

$$+\int_{\Gamma_\mathrm{opt}} \frac{\gamma_\mathrm{N}\mu}{h} (\boldsymbol{u} - \boldsymbol{u}_\mathbf{BC}) \cdot \boldsymbol{v} \mathrm{d}s \,. \tag{17}$$

This formulation enables optimization, but it does not ensure that the control $\boldsymbol{u}_\mathrm{BC}$ remains within physically reasonable bounds. Therefore, a regularization term with penalty parameter α was added to the cost functional to limit the total flow through Γ_opt and to penalize large values of $|\boldsymbol{u}_\mathrm{BC}|$. Moreover, for safety reasons, only injection of the highly reactive hydrogen-air mixture is feasible in experiments, whereas suction is not permitted. To enforce this constraint, a second penalty term, weighted with β, was introduced. The adapted cost functional used in the BC optimization

$$\tilde{J} = J + \int_{\Gamma_\mathrm{opt}} \alpha \boldsymbol{u}_\mathrm{BC} \cdot \boldsymbol{u}_\mathrm{BC} \mathrm{d}s + \int_{\Gamma_\mathrm{opt}} \beta \boldsymbol{u}_\mathrm{BC} \cdot \boldsymbol{n} \mathrm{d}s \tag{18}$$

$$= J + J_{|\boldsymbol{u}_\mathrm{BC}|} + J_{\boldsymbol{u}_\mathrm{BC}\cdot\boldsymbol{n}<0} \,. \tag{19}$$

Results

Figure 3 shows the cost functional over iterations for an optimization where $\beta \neq 0$, i.e., with a restriction to injection. The bulk velocity at the inlet was reduced by 10%, corresponding to roughly 10% of the mass flow passing through Γ_opt. At around iteration 90, oscillations appear in the trace of $J_{\boldsymbol{u}_\mathrm{BC}\cdot\boldsymbol{n}<0}$ and J, likely due to their opposing directions of descent.

For an intermediate step at iteration 80 and for the final iteration, the control $\boldsymbol{u}_\mathrm{BC}$ is illustrated in Fig. 2. The intermediate result shows a better restriction to injection. However, because $J_{\boldsymbol{u}_\mathrm{BC}\cdot\boldsymbol{n}<0}$ is equipped with a sign, local peaks of high $\boldsymbol{u}_\mathrm{BC}$ appear, since these decrease $\tilde{J}$. A promising solution would be to enforce equality and inequality constraints

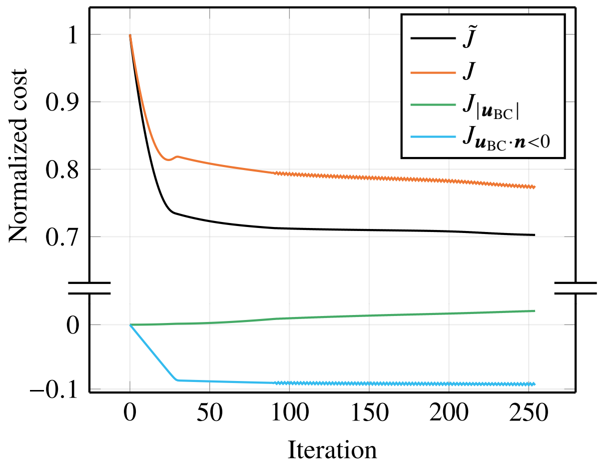

Figure 3: Trace of the cost functional values over iterations for the BC optimization. Both magnitude and sign penalty of $\boldsymbol{u}_{\mathrm{BC}}$ are active. The costs are normalized with the initial value of J at iteration 0.

with an augmented Lagrangian method (see, e.g., Toussaint, 2014). This would also eliminate free parameters α and β in Eq. (18) and the need for manual tuning. As the optimization goes on, fluid is accelerated abruptly into the boundary layer at the end of Γ_{opt}. Eventually, $\boldsymbol{u}_{\mathrm{BC}}$ grows noisier because of mesh-dependent sensitivities, and the optimization is manually aborted. This suggests the use of parameterized distributions in future optimizations.

Although J was reduced by about 20% during the optimization, the axial velocity in the boundary layer did not increase. Instead, most of the reduction was obtained by bringing $\boldsymbol{u}$ closer to $\boldsymbol{u}_{\mathrm{g}}$ along the centerline. This behavior persists even when suction is allowed ($\beta = 0$) and when α is varied such that up to 16% of the total mass flow passes through Γ_{opt}. A likely reason is the relatively large size of Γ_{opt}, which distributes the control flow over a wide area and therefore yields low-momentum actuation. A possible remedy would be to restrict Γ_{opt} to a narrow slit so that the same mass flow produces higher velocities and, consequently, jets with greater momentum.

SHAPE OPTIMIZATION

Methods

The assembled $\frac{dJ}{d\boldsymbol{a}}$ often has unfavorable properties, such as noise. In the BC optimization, an H^1 projection was used to ensure some smoothness of the control. However, in the case of mesh-deforming SO, this does not suffice, since using the gradient as a direction of descent could move the mesh nodes such that the mesh quality deteriorates. Over iterations, this could lead to the need for re-meshing or an ultimate failure of the optimization. To counter this, the descent direction must be carefully altered to preserve mesh quality while still being a guaranteed direction of descent. We chose a solution in which the mesh is understood as a linear elastic solid body that is subject to the force $\frac{dJ}{d\boldsymbol{a}}$ and deforms accordingly following Schulz & Siebenborn (2016). This deformation is often referred to as gradient deformation $\boldsymbol{g}$ and solves:

Find $\boldsymbol{g} \in H^1_{\Gamma_{\mathrm{fix}}}(\Omega_{\mathrm{opt}})^d$ such that

$$\int_{\Omega_{\mathrm{opt}}} 2\mu_{\boldsymbol{g}} \mathrm{sym}(\nabla \boldsymbol{g}) : \mathrm{sym}(\nabla \boldsymbol{v}) \mathrm{d}x = \frac{dJ}{d\boldsymbol{a}} \cdot \boldsymbol{v} \qquad (20)$$

for all $\boldsymbol{v} \in H^1_{\Gamma_{\mathrm{fix}}}(\Omega_{\mathrm{opt}})^d$.

Here, the bilinear form on the left-hand side $a_\Omega(\boldsymbol{g}, \boldsymbol{v})$ models a simplified linear elastic body with one of the Lamé parameters set to zero. To prevent mesh motion from propagating into the non-optimized domain, the deformation is required to vanish on the fixed walls $\Gamma_{\mathrm{fix}} = \partial\Omega_{\mathrm{opt}} \setminus \Gamma_{\mathrm{opt}}$. Hence, the deformation space is chosen as $H^1_{\Gamma_{\mathrm{fix}}}(\Omega_{\mathrm{opt}})^2$. In addition, this choice yields a coercive form a_Ω and thereby ensures that $\boldsymbol{g}$ is a guaranteed descent direction (see, e.g., Blauth, 2021). To further enhance mesh quality, a stiffness field $\mu_{\boldsymbol{g}}$ is introduced that is high in areas where large deformations are expected and small in areas where small deformations are expected. In our case, $\mu_{\boldsymbol{g}}$ was a linear distribution from $\mu_{\boldsymbol{g},\mathrm{max}} = 4{,}000$ at Γ_{opt} to $\mu_{\boldsymbol{g},\mathrm{min}} = 1{,}000$ at Γ_{sym}, but for more complex cases, it can be lifted into the domain by solving a Poisson problem.

Results

As shown in Fig. 4, the cost functional decreases by approximately 55% over the iterations. The corresponding shapes of Γ_{opt} at three equally spaced iterations (SO-1 to SO-3) illustrate its continuous evolution toward a diverging-converging nozzle. Extending Ω_{opt} further upstream led to similar optimized geometries. At the end of the optimization, the mesh

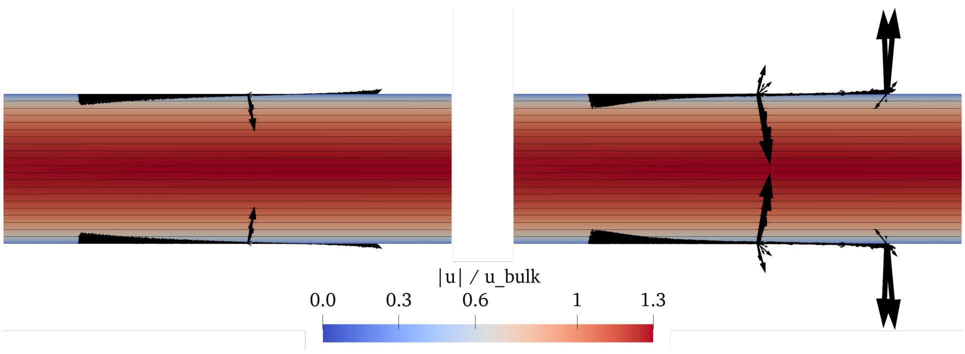

Figure 2: Intermediate (iteration 80, left) and final (right) BC optimization results. Color denotes the velocity magnitude, with streamlines overlaid. The arrows represent the distributed boundary forcing $\boldsymbol{u}_{\mathrm{BC}}$ on Γ_{opt}, where the maximum arrow length corresponds to $1.5\,\mathrm{m/s} = 0.25 u_{\mathrm{bulk}}$. Even though β is large enough to ensure significant contribution of $J_{\boldsymbol{u}_{\mathrm{BC}}\cdot\boldsymbol{n}<0}$ to $\tilde{J}$, some parts of $\boldsymbol{u}_{\mathrm{BC}}$ point outward since penalty methods rely on slight constraint violation.

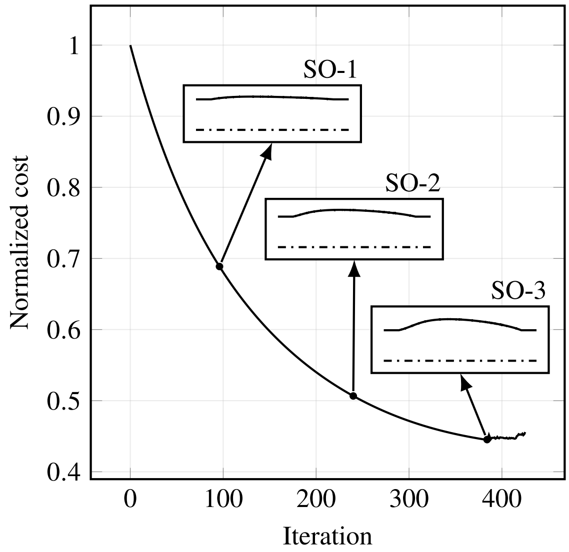

Figure 4: Cost J over iterations of the SO. The cost is normalized with the initial value of J. At three points the evolution of Γ_{opt} from a strait line at the iteration zero to the optimized shape is shown with the axis of symmetry z given as a dashed line for reference. At the end of the optimization the mesh quality begins to deteriorate and the optimization is manually aborted.

quality begins to deteriorate at the nozzle exit and ripples on Γ_{opt} appear. This effect is even more drastic when computing $\frac{dJ}{d\boldsymbol{a}}$ in the volume form. Then, additionally, the boundary layer mesh is stretched, hinting at sensitivities that are not mesh-independent. These issues will be addressed in the future by smoothing the sensitivity over multiple elements prior to computing $\boldsymbol{g}$.

Figure 5 shows contours of k with overlaid streamlines of $\boldsymbol{u}$ for the final optimization result SO-3. The optimized nozzle first decelerates the flow in the divergent section and then accelerates it in the converging section, thereby directing high-momentum fluid into the boundary layer. As a result, the velocity profile exhibits very high wall-normal gradients. Up to the dump plane Γ_{d}, the profile gradually redevelops toward a turbulent pipe flow, but it remains closer to the target profile $\boldsymbol{u}_{\mathrm{g}}$ than the baseline profile in the mixing tube. The figure also indicates elevated production of k caused by shear and flow acceleration.

EXPERIMENTAL ANALYSIS

Due to the better performance of the SO compared to the BC optimization, the baseline shape, SO-1, SO-2, and SO-3 were 3D-printed and experimentally investigated. For each of the shapes, the experimental burner was operated at various Reynolds numbers from Re = 7,857, i.e., close to the operational point of the SO, and up to Re = 9,867 under atmospheric conditions. At stable operating points the flame anchors close to Γ_{d} in the combustion chamber.

To assess how the shapes SO-1 to SO-3 affect FB onset, FB limits were measured at three different operating points defined by different air mass flow rates. At each operating point, the air mass flow rate was kept constant, while the hydrogen mass flow rate was increased in small increments, thereby raising the equivalence ratio ϕ and, with it, the mixture reactivity. After each increment, the thermal equilibrium indicated by temper-

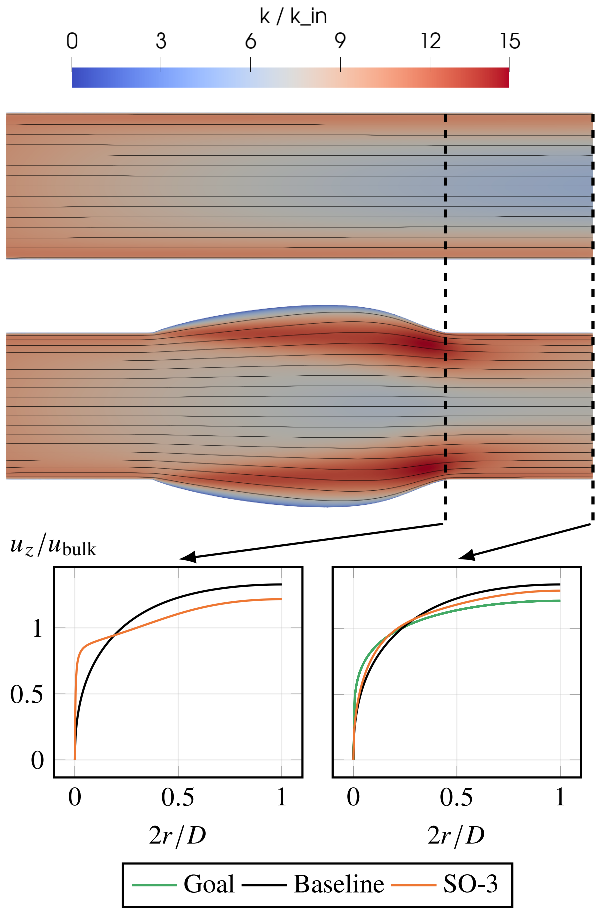

Figure 5: Contours of the turbulent kinetic energy k and streamlines of the baseline and shape-optimized mixing tube. Profiles of u_z are shown for both shapes at the end of the optimized region and at the dump plane Γ_{d}.

ature sensors was awaited before the fuel mass flow rate was increased further. FB was identified by thermocouples inside the combustor, which detected the temperature rise associated with the upstream movement of the flame. Across all experiments, the thermal power ranged from 3.4 kW to 5.6 kW.

Figure 6 shows the FB limits, defined as the highest equivalence ratio ϕ at which the flame remained stable, as a function of Re, based on the mixture properties. All shapes increased the FB limit by up to $\Delta\phi \approx 0.1$, although the effect occurred at different Re. The least deformed shape, SO-1, increased the FB limit at low Re, then exhibited a drop-off and increased it again at high Re. SO-2 showed a similar drop-off, but only at the highest Re. In contrast, SO-3 increased the FB limit only at higher Re. At least two mechanisms may be involved. At lower velocities, the less deformed shapes may produce flow modifications that remain close to those predicted by the standard k-ε model and thus increase the near-wall flow rate. More strongly deformed shapes, in contrast, may cause flow separation in the diverging nozzle section and therefore fail to produce the beneficial profile changes predicted numerically. In all cases, however, the modified shapes increase k relative to the straight mixing tube, as shown in Fig. 5. This may enhance near-wall mixing and cooling, which Jaeschke *et al.* (2026) showed to be key mechanisms in mitigating FB. Future hot-wire measurements near Γ_{d} will be used to determine k and $|\boldsymbol{u}|$ profiles.

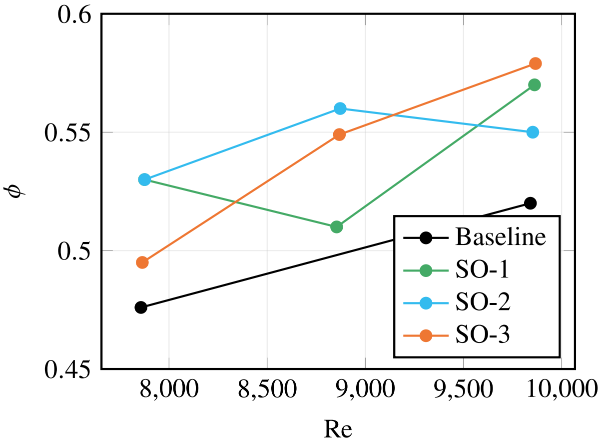

Figure 6: Experimental FB limit measurements of the shape-optimized mixing tubes. For a given Re, the graph shows the critical equivalence ratio ϕ at which FB occurs. Through the SO, FB is shifted by 4-11% ϕ in relation to the baseline geometry.

CONCLUSION

This work presented boundary condition optimization and shape optimization of a mixing tube for the cold-flow configuration of a hydrogen burner at Re = 7,840. The optimization was based on automatically and symbolically derived adjoint sensitivities, using Nitsche's method for differentiable Dirichlet boundary conditions and an analogy to linear elasticity for mesh deformation. In both optimizations, the objective was to increase the wall-velocity gradient while reducing the centerline velocity at the dump plane. First experiments for the shape optimization indicate a shift of the flashback limits by more than 11% in equivalence ratio, demonstrating the potential of the approach. Since the performance varies across operating points, further cold-flow experiments are required to clarify the flow changes induced by the shape optimization. Moreover, the standard k-ε turbulence model is invalid at the wall, which renders the results uncertain and motivates a wall correction in future work. Beyond the present study, sensitivity-based analyses of flow instabilities offer a promising perspective for flashback mitigation, as both low-frequency eigenmodes (Douglas *et al.*, 2023) and low-velocity boundary-layer streaks (Porath *et al.*, 2025) have been linked to flashback. Accordingly, future work will focus on implementing resolvent analysis to suppress these low-velocity streaks and thereby further reduce flashback risk (von Saldern *et al.*, 2025).

ACKNOWLEDGMENT

This work has been conducted as part of the joint research project ENERGIZE (Adjoint-based and additive manufacturing-enabled optimization of hydrogen combustion systems) within the scope of the SPP2419 HyCAM and is supported by the German Research Foundation (DFG) under grant number 523881008. Furthermore, the authors would like to thank Lukas Melzig for his support in manufacturing the mixing tubes for the experimental investigation.

REFERENCES

2009 *ANSYS FLUENT 12.0 User's Guide*. ANSYS, Inc., release 12.0, help system.

2024 *OpenFOAM v2412*. OpenCFD Ltd., open source CFD software, version v2412.

Alnæs, Martin S., Logg, Anders, Ølgaard, Kristian B., Rognes, Marie E. & Wells, Garth N. 2014 Unified form language: A domain-specific language for weak formulations of partial differential equations. *ACM Transactions on Mathematical Software* **40** (2), 1–37.

Baratta, Igor A., Dean, Joseph P., Dokken, Jørgen S., Habera, Michal, Hale, Jack S., Richardson, Chris N., Rognes, Marie E., Scroggs, Matthew W., Sime, Nathan & Wells, Garth N. 2023 DOLFINx: The next generation FEniCS problem solving environment.

Blauth, Sebastian 2021 Adjoint-based shape optimization and optimal control with applications to microchannel systems. Doctoral thesis, Fraunhofer-Institut für Techno- und Wirtschaftsmathematik.

Cossu, Carlo 2014 An Introduction to Optimal Control. *Applied Mechanics Reviews* **66** (2), 024801.

Douglas, Christopher M., Polifke, Wolfgang & Lesshafft, Lutz 2023 Flash-back, blow-off, and symmetry breaking of premixed conical flames. *Combustion and Flame* **258**, 113060.

Jaeschke, Alexander, Kaiser, Thomas Ludwig, Melzig, Lukas, Zaeh, Michael F., Oberleithner, Kilian & Paschereit, Christian Oliver 2026 Effect of additively manufactured wall lattice structures on flashback limits in a hydrogen jet flame combustor. In *Proceedings of the ASME Turbo Expo 2026*. Milan, Italy: ASME, to appear.

Jones, W.P & Launder, B.E 1972 The prediction of laminarization with a two-equation model of turbulence. *International Journal of Heat and Mass Transfer* **15** (2), 301–314.

Kalantari, Alireza & McDonell, Vincent 2017 Boundary layer flashback of non-swirling premixed flames: Mechanisms, fundamental research, and recent advances. *Progress in Energy and Combustion Science* **61**, 249–292.

Kontogiannis, Alexandros, Elgersma, Scott V, Sederman, Andrew J & Juniper, Matthew P 2025 Bayesian inverse Navier–Stokes problems: joint flow field reconstruction and parameter learning. *Inverse Problems* **41** (1), 015008.

Kuzmin, D., Mierka, O. & Turek, S. 2007 On the implementation of the $k-\varepsilon$ turbulence model in incompressible flow solvers based on a finite element discretisation. *International Journal of Computing Science and Mathematics* **1** (2/3/4), 193.

Pope, Stephen B. 2015 *Turbulent flows*, 1st edn. Cambridge: Cambridge Univ. Press.

Porath, P., Altenburg, L.A., Klein, S.A., Tummers, M.J. & Ghani, A. 2025 Low velocity streaks combined with intrinsic flame instabilities provoke boundary layer flashback in a turbulent premixed jet-stabilized hydrogen flame. *Combustion and Flame* **278**, 114236.

Salama, Amgad 2021 Velocity Profile Representation for Fully Developed Turbulent Flows in Pipes: A Modified Power Law. *Fluids* **6** (10), 369.

von Saldern, Jakob G.R., Beuth, Jan Paul, Reumschüssel, Johann Moritz, Jaeschke, Alexander, Paschereit, Christian Oliver & Oberleithner, Kilian 2025 Low-frequency streaky structures in turbulent hydrogen jet flames. *Combustion and Flame* **278**, 114231.

Schulz, Volker & Siebenborn, Martin 2016 Computational Comparison of Surface Metrics for PDE Constrained Shape Optimization. *Computational Methods in Applied Mathematics* **16** (3), 485–496.

Toussaint, Marc 2014 A novel augmented lagrangian approach for inequalities and convergent any-time non-central updates.